Chapter I.1
Principles of Radiometric Remote Sensing of the Troposphere

Domenico Cimini and Ed R. Westwater

1 Introduction

Surface-based radiometric measurements of natural radiation are useful in a variety of applications, including planetary energy budget, meteorological observations and forecasting, climate benchmarking and model parameterization, satellite validation, and fundamental physics. One reason for the utility of these measurements is that with careful design, radiometers can be operated in a long-term unattended mode in nearly all weather conditions (Hogg et al., 1983; Philippona et al., 1995; Knuteson et al., 2004a, b). An important feature is the nearly continuous observational capability on time scales of seconds to minutes. The measurements with calibrated radiometers can enable the continued development of absorption and radiative transfer models in both clear (Liebe, 1989; Rosenkranz, 1998; Clough et al., 2005), cloudy (Liebe et al., 1991), and precipitating (Marzano et al., 2005; Battaglia et al., 2009) atmospheres. In addition, the continued development of retrieval and data assimilation algorithms (Clothiaux et al., 2000; Rodgers, 2000) provides more accurate and new products, combining radiometric observations with external data sources, such as forecasts or soundings from active sensors. This contribution gives an overview of some applications of ground-based radiometry in the electromagnetic spectrum from the visible (VIS) to microwave (MW) ranges for the remote sensing of troposphere.

2 Physical Principles

Passive ground-based remote sensing instruments rely on measurements of solar radiation transmitted through the atmosphere and of thermal radiation, both infrared and microwave, emitted by the atmosphere. The basic ideas of natural emission of electromagnetic (EM) radiation and radiative transfer are given in Liou (1980),

D. Cimini (✉)
IMAA/CNR, C.da S. Loja, Tito Scalo (PZ), Italy
e-mail: cimini@imaa.cnr.it

D. Cimini et al. (eds.), *Integrated Ground-Based Observing Systems*,
DOI 10.1007/978-3-642-12968-1_1, © Springer-Verlag Berlin Heidelberg 2010

Goody and Yung (1995), and Petty (2006) and their application to radiometric remote sensing is outlined in Elachi (1987) and Stephens (1994).

The radiatively significant atmospheric constituents are gas molecules, aerosol particles, and water in the form of cloud droplets, ice crystals, and precipitation. Because the transmission and emission depend on specific properties of the atmosphere, one can use these passive measurements to analyze the state of the atmosphere.

2.1 Radiation Quantities

Several quantities are commonly used to describe and quantify the main properties of EM radiation; these are summarized herewith with the corresponding physical units in the International Standard System. The energy carried by an EM wave is called radiant energy [Joule]; the time rate at which radiant energy passes a certain location is called wave power or radiant flux [Watt]. The wave power or radiant flux intercepted by a unit area of a plane surface is the radiant flux density [W/m^2] but it is usually called irradiance for flux incident upon the surface or emittance for flux leaving the surface. The radiant flux density illuminating (irradiance) or emerging from (emittance) an extended object in a given direction per unit projected area is called radiation intensity [W/m^2 st], which is often called radiance. Thus, the radiance expresses the EM wave power per unit projected area per unit solid angle. All the radiation quantities have equivalent spectral quantities, which are function of the EM wavelength, describing each quantity in a given wavelength interval, called spectral width or bandwidth. For example, the spectral radiance expresses the EM wave power per unit projected area per unit solid angle per unit wavelength interval [W/m^2 st m].

2.2 Extinction, Transmission, and Emission

When a monochromatic EM wave propagates through an homogeneous medium, it interacts with matter. The radiation may be attenuated by the absorption from the medium (conversion of radiation energy into heat or chemical energy) or scattered (redirection of radiation out of the original direction of propagation). The residual radiation at any point of the medium is called the transmitted radiation up to that point. However, the medium may also enhance the radiation intensity by thermal emission (conversion of thermal or chemical energy into radiation energy) or by scattering (redirection of isotropic radiation into the considered direction of propagation).

For energy conservation, the sum of the absorbed, transmitted, and scattered radiation energy must be equal to the incident energy. Thus, calling I_{i} the incident radiant flux intensity and I_{a}, I_{s}, and I_{t} the radiant flux intensity as absorbed, scattered, and transmitted by the medium, respectively, then

$$I_{\mathrm{a}} + I_{\mathrm{s}} + I_{\mathrm{t}} = I_{\mathrm{i}}. \tag{1}$$

This equation can be written in terms of the unitless quantities absorptance A, reflectance R (in analogy with a reflecting surface), and transmittance T, just by diving for I_i:

$$A + R + T = 1. \tag{2}$$

2.2.1 Atmospheric Extinction

Consider the passage of radiation of wavelength λ through a infinitesimal layer of air ds, measured along the direction of propagation. If the intensity is initially I, and calling β_e the extinction coefficient, then the reduction in I due to extinction is

$$dI_e = -\beta_e I ds. \tag{3}$$

The relative contributions of scattering and absorption to the total extinction are given by the additive scattering and absorption coefficients:

$$\beta_e = \beta_a + \beta_s, \tag{4}$$

while the relative importance of scattering versus absorption is given by the single scattering albedo, defined as

$$\omega = \beta_s/\beta_e = \beta_s/(\beta_a + \beta_s). \tag{5}$$

In the equations above, it is the extinction coefficient β_e that links absorption and scattering to the composition of the atmosphere.

Gaseous Absorption

When the radiant energy is absorbed/emitted by a gas molecule, there must be a corresponding increase/decrease of its internal energy. In particular, the internal energy may change in the presence of a change in translational kinetic energy, rotational kinetic energy, vibrational energy, and/or distribution of electric charge within the molecules.

The energy carried by photons in the EM spectrum considered here covers the range from 10^{-23} J at microwaves to 10^{-18} J at the ultraviolet (UV) edge. Therefore, different wavelength bands lead to different types of transitions, associated with different modes of energy storage. For example, transitions between rotational states usually involve low-energy photons, i.e., infrared (IR) and MW, because rotational states of most molecules are close in energy. Low-energy transitions often occur simultaneously with higher energy transitions, giving a fine scale structure to the total absorption spectrum.

- *Rotational* transitions may occur in the interaction of an EM wave with molecules possessing either a magnetic or a electric dipole, so that the externally applied magnetic field can exert a torque on the molecule. Thus, atmospheric molecules that present neither an electric nor a magnetic dipole (such as N_2) have no rotational spectrum. Rotational absorption bands are associated with low-energy transition and thus are located in the far infrared to microwave spectrum. Oxygen has no electric dipole but it does have a permanent magnetic dipole moment, which causes rotational absorption bands at 60 and 118 GHz. All other atmospheric molecules exhibit permanent electric dipole and thus rotational absorption bands.

- *Vibrational* transitions are associated with considerably larger energies than rotational transition, giving rise to absorption/emission lines in the thermal and near IR bands. However, vibrational and rotational transitions may occur simultaneously, resulting in a more complex absorption spectrum, with additional transitions slightly more or less energetic than that of a pure vibrational transition.
- *Electronic* transitions happen when a photon is absorbed/emitted in association with an electron changing its orbit in the molecule. For the EM spectrum considered here, typically the outermost electrons are of interest, since transitions between the ground state and the first excited state are associated with wavelengths in the near IR, visible, and UV bands.

The combination of all three modes of excitation leads to a set of discrete energy levels forming the total absorption line spectrum. In addition, there are three distinct processes, whose relative importance depends on local environmental conditions, that cause the broadening of the line absorption, permitting a given atmospheric constituent to absorb radiation not only at the nominal wavelength but also in an interval around it. These three processes are natural, Doppler, and pressure broadening.

- The natural broadening is a consequence of the Heisenberg uncertainty principle; it is negligible compared to the other two throughout most of the atmosphere.
- The Doppler broadening is caused by the translational motions of individual molecules which slightly shift the transitions wavelengths randomly. This broadening becomes important in the upper atmosphere only.
- The pressure broadening is caused by the collisions between molecules which perturb the natural transitions between energy states. The pressure broadening is the primary mechanism in the troposphere, where collisions occur with very high frequency.

For the purpose of this overview, the pressure broadening is usually described adequately by the Lorentz line shape. Note that the Lorentz line shape is known to underestimate the effect of the far wings contributions. Another limitation is that the Lorentz model is only valid when the line width is very small compared to the center frequency. Thus, in the microwave band, the preferred line model is the van Vlack–Weisskopf function (Petty, 2006). An example of the pressure broadening effect on line absorption is evident on the rotovibrational oxygen complex from 50 to 70 GHz; individual lines are evident for pressure below 100 mb, while they form a nearly continuous absorption band at surface pressures.

Outside the major resonant absorption lines some level of absorption is generally found that does not exhibit line-like structure. This feature is known as continuum absorption (since it varies slowly with wavelength) and results from three causes: photoionization, photodissociation, and longwave continuum absorption. The first two affect primarily the short wavelength edge (UV) of the considered spectrum and refer to high energetic photons that can extract an electron from an atom (ionization) or break a molecule (dissociation). The third cause affects spectral windows throughout the IR and MW regions and it is due primarily to water vapor. Although its mechanism is not completely understood, it is probably due to a combination of the far wing contributions of shorter wavelength lines and/or to the formation of H_2O molecule clusters that exhibit far more complex vibrational and rotational transitions (which tend to a continuum) than the isolated molecules.

Atmospheric Scattering

Apart from the atmospheric absorption, the extinction of radiation propagating in atmosphere happens through scattering of radiation. In order to formulate quantitatively the effect of scattering, the angular distribution of the scattered radiation must be specified. This is described by the scattering phase function $p(\cos\alpha)$ where α is the angle between the incident and scatted radiation. The simplest case is when the scattering is isotropic, then $p(\cos\alpha) = \text{constant}$. In general, the phase function can be written as a series of Legendre polynomials and is often rather complex. For practical applications it is useful to introduce the asymmetry parameter g, which may be interpreted as the average value of $\cos\alpha$for a large value of scattered photons, as

$$g = \frac{1}{4\pi} \int_{4\pi} p(\cos\alpha) \cos\alpha d\Omega. \tag{6}$$

Note that $-1 \leq g \leq 1$ and in general $g > 0$ implies preferential scattering in the forward direction, $g < 0$ implies scattering in the backward direction, while $g = 0$ corresponds to isotropic scattering. In terms of g, the phase function may be modeled with the Henyey–Greenstein phase function

$$p_{\mathrm{HG}}(\cos\alpha) = \frac{1 - g^2}{(1 + g^2 - 2\,g\cos\alpha)^{3/2}}\ . \tag{7}$$

Any atmospheric constituent (gas and particles) may be seen as a scatterer of EM radiation, strongly depending on its size, shape, and composition. It is usually useful to introduce the nondimensional size parameter:

$$x = \frac{2\pi r}{\lambda} \tag{8}$$

in which r is the radius of a spherical particle or of a sphere having the same volume of the particle. This assumption is usually appropriate for most of the atmospheric constituents, such as molecules, cloud droplets, and rain, but it is rather crude for ice crystals, snowflakes, and solid-phase aerosols. In general, particles that are far smaller than the wavelength will scatter only weakly (though they may still absorb

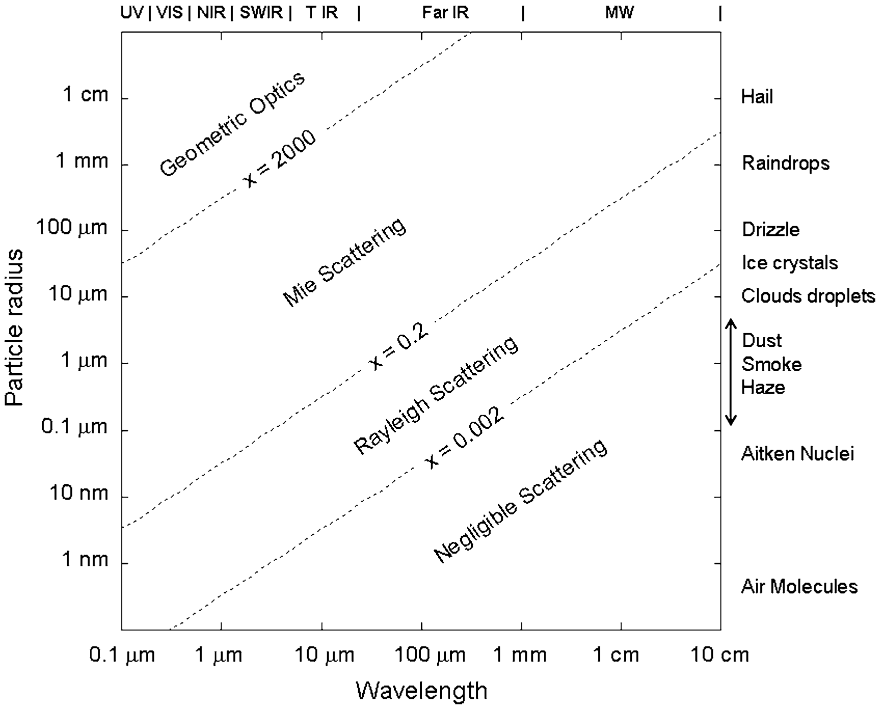

Fig. I.1.1 Relationship between particle size, radiation wavelength, and scattering behavior (adapted from Petty, 2006)

radiation). On the other hand, particles that are very large compared to the wavelength of radiation will interact with radiation following the laws of geometric optics for homogeneous media. For other particles falling in between the two extremes above, more complex methods are needed to compute their scattering properties. Given the size of a particle and the incident wavelength (and thus, the value of x), it can be readily determined whether scattering is likely to be significant and which scattering regime is most applicable (Rayleigh, Mie, or geometric optics), as pictured in Fig. I.1.1. Finally, the particle composition affects the scattering properties through the relative index of refraction with respect to air, which in turn is a function of wavelength.

Scattering by Atmospheric Molecules

In clear air, i.e., in the absence of clouds and aerosols, it is mostly absorption by gas that controls the atmospheric extinction. However, at shorter wavelengths (visible and UV), air molecules can significantly scatter radiation.

When a particle is sufficiently small relative to incident wavelength, i.e., $x \ll 1$, the whole particle experiences simultaneously the same externally imposed oscillating electric field and becomes partially polarized. This corresponds to the classical model for interpreting the Rayleigh scattering, which leads to the following phase function and scattered intensity:

$$p(\cos\alpha) = \frac{3}{4}(1 + \cos^2\alpha), \tag{9}$$

$$I \propto \frac{1}{\lambda^4}(1 - \sin^2\alpha\cos^2\varphi), \tag{10}$$

where φ is the polar angle of the incident radiation taken from an arbitrary starting direction. Thus, in the Rayleigh scattering regime the intensity of scattered radiation is inversely proportional to the fourth power of the radiation wavelength. Calling m the relative refraction index of the particle with respect to the surrounding medium, the absorption and scattering efficiencies, respectively, are

$$Q_\mathrm{a} = 4x\Im\left(\frac{m^2 - 1}{m^2 + 2}\right), \tag{11}$$

$$Q_\mathrm{s} = \frac{8}{3}x^4\left|\frac{m^2 - 1}{m^2 + 2}\right|^2, \tag{12}$$

where $\Im$ indicates the imaginary part of a complex number. Noting that Q_a is proportional to x while Q_s to x^4, it follows that for sufficiently small particles, like molecules, assuming a complex relative index of refraction (otherwise $Q_\mathrm{e} = 0$), $Q_\mathrm{s} << Q_\mathrm{a} \sim Q_\mathrm{e}$. Therefore, for sufficiently small particles with complex refractive index, scattering is negligible and absorption is proportional to mass path only. As sketched in Fig. I.1.1, atmospheric molecules exhibit negligible scattering for wavelength longer than visible and exhibit Rayleigh scattering in the visible-to-UV range.

Scattering and Absorption by Atmospheric Particles

In addition to the gas molecules, there is a large variety of particles floating in the atmosphere, including cloud droplets, ice crystals, rain drops, snowflakes, smoke, dust, and pollen. The typical size of these particles ranges from fraction of a micrometer to a few centimeters. Depending on the size and composition these particles can scatter and/or absorb radiation. The rigorous theory of Mie can be used for dielectric spheres of arbitrary size, which leads to the following absorption and scattering efficiencies:

$$Q_\mathrm{e} = \frac{2}{x^2}\sum_{n=1}^{\infty}(2n + 1)\Re(a_n + b_n), \tag{13}$$

$$Q_\mathrm{s} = \frac{2}{x^2}\sum_{n=1}^{\infty}(2n + 1)\left(|a_n|^2 + |b_n|^2\right), \tag{14}$$

where $\Re$ indicates the real part of a complex number and the coefficients a_n and b_n are referred to as Mie scattering coefficients, which are functions of x and m.

For $x = 0$, the asymmetry parameter g is also zero, as in the Rayleigh regime. As x increases, g increases very rapidly up to a plateau at about 0.8–0.95; this indicates that particles comparable to or larger than the wavelength tend to strongly forward scattering. The Mie solution yields results that converge to the geometric optics for large x values (i.e., >50) and to Rayleigh solution for small x values (<0.6).

For any particle type, usually there will be a combination of sizes given by the particle size distribution function $n(r)$ (number of particles of radius r per unit volume of air). The volume extinction coefficient (and analogously for the scattering and absorption coefficients) for the distribution of particles described by $n(r)$ is

$$\beta_\mathrm{e} = \int_0^\infty n(r) Q_\mathrm{e}(r) \pi r^2 dr. \tag{15}$$

As sketched in Fig. I.1.1, the Rayleigh regime is valid at microwave wavelengths for particles as large as raindrops. In the Rayleigh regime, a cloud behaves like an homogeneous medium rather than a collection of discrete scatterers. Clouds in the visible band strongly scatter sunlight but absorb very little, practically zero. Smoke on the other hand absorbs strongly visible radiation.

2.2.2 Atmospheric Transmission

The fall off of the radiation intensity at wavelength λ as a function of the geometric distance along an arbitrary propagation direction s can be expressed as

$$I_\lambda(s) = I_\lambda(0) \exp(-\beta_\mathrm{e}(\lambda) s). \tag{16}$$

Considering an infinitesimal distance ds over which the extinction coefficient may be assumed constant, the equation above leads to Eq.(3), rewritten here as

$$dI_\lambda(s) = -I_\lambda(s) \beta_\mathrm{e}(\lambda, s) ds. \tag{17}$$

By integrating we obtain a general form of the Beer's law:

$$I_\lambda(s_\mathrm{b}) = I_\lambda(s_\mathrm{a}) \exp\left(-\int_{s_\mathrm{a}}^{s_\mathrm{b}} \beta_\mathrm{e}(\lambda, s) ds \right). \tag{18}$$

The integral quantity is called the optical depth (or thickness) τ_λ from which we obtain the atmospheric transmittance:

$$T_\lambda(s_\mathrm{a}, s_\mathrm{b}) = e^{-\tau_\lambda(s_\mathrm{a}, s_\mathrm{b})}. \tag{19}$$

In a plane parallel approximation of the atmosphere, which assumes that the extinction coefficient depends only on the vertical distance z, the optical thickness becomes

$$\tau_\lambda(z_a, z_b) = \int_{z_a}^{z_b} \beta_e(\lambda, z)dz \tag{20}$$

and the transmission for the radiation propagating with direction $\mu \equiv |\cos\vartheta|$, where ϑ is the angle of propagation relative to the zenith direction, is

$$T_\lambda(z_a, z_b) = \exp\left(-\frac{\tau_\lambda(z_a, z_b)}{\mu}\right). \tag{21}$$

The atmosphere is composed of a mixture of gases and particles (hydrometeors and aerosols) which have the capacity to absorb and/or scatter radiation in different ways at different spectral bands. In general, both absorption and scattering concur in attenuating the radiation traveling through the atmosphere. The total volume extinction coefficient (and analogously for the scattering and absorption coefficients) for the atmosphere is the sum of the corresponding coefficients for the individual components $\beta_e(\lambda) = \sum_i \beta_{e,i}(\lambda)$, where i indicates the ith constituent.

The overall transmittance of the cloud-free and aerosols-free atmosphere is controlled primarily by absorption due to constituent gases. In fact, in the absence of particles in the atmosphere, the extinction is largely dominated by the gaseous absorption; however, at visible and shorter wavelengths, air molecules significantly scatter the EM radiation. The scattering cross section is approximately proportional to λ^4 and thus it is stronger in the UV while becomes almost negligible in the IR.

The characteristics of cloud-free and aerosols-free atmospheric transmission for the EM spectrum from UV to MW are shown in Fig. I.1.2. Note that the transmittance was computed for a standard mid-latitude atmosphere; in a much drier (moister, respectively) environment the water vapor amount would be much less (more) so that the atmosphere would be substantially more (less) transparent in the H_2O absorption bands. Starting in the UV band, we see that the atmosphere is almost completely opaque to radiation with $\lambda < 0.3$ μm, due to oxygen and ozone absorption. Conversely, the atmosphere is quite transparent throughout most of the visible band ($0.4 < \lambda < 0.7$ μm). From 0.7 to 4 μm, in the near IR (NIR) and shortwave IR (SWIR) regions, the atmosphere presents many features due to the absorption of mostly water vapor (WV) and in less extent CO_2, CH_4, N_2O. Through the thermal IR (TIR) band, from 4 to 50 μm, the atmosphere presents broad bands of near-total absorption due to CO_2 (near 4 μm), H_2O (from 5 to 8 μm), ozone (near 9.6 μm), and again CO_2 ($\lambda > 13$ μm) as well as fairly transparent bands, so-called atmospheric windows (8–13 μm). From 50 μm to 1 mm, the far IR range, the atmosphere is almost completely opaque due to the strong absorption of H_2O. At longer wavelengths, in the microwave region from 1 to 100 mm (300 to 3 GHz), the atmospheric

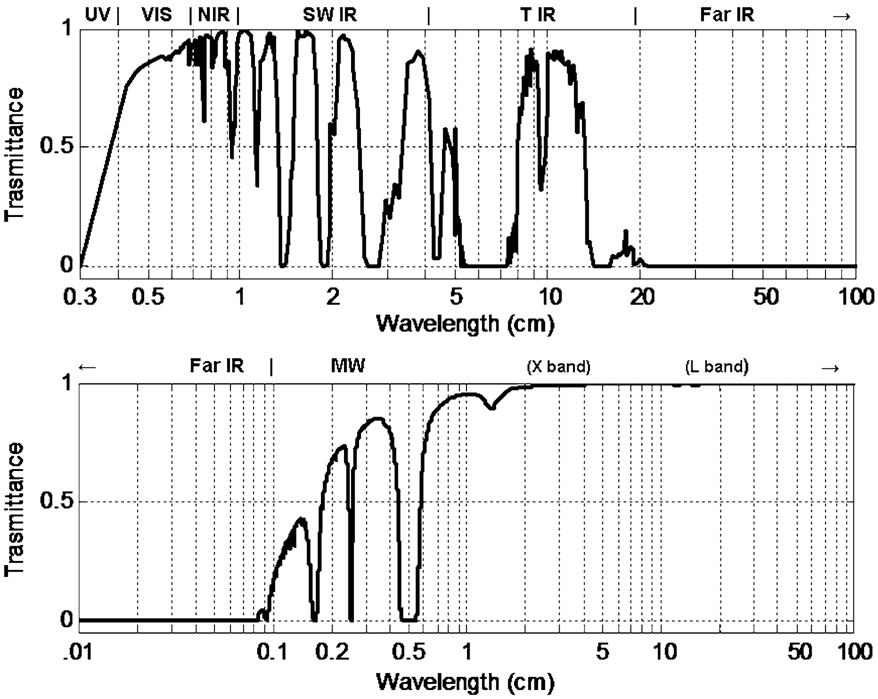

Fig. I.1.2 Transmission of cloud-free and aerosols-free atmosphere from the UV to the MW range. Calculations were made with a line-by-line radiative transfer code for a standard mid-latitude atmosphere (adapted from Elachi, 1987; data courtesy of Tiziano Maestri, University of Bologna)

absorption is dominated by water vapor and oxygen contributions. In particular, the atmosphere is increasingly transparent with longer wavelengths, due to the wing of strong WV absorption in the far IR, except that WV presents selective absorption near 183 and 22 GHz ($\lambda \sim 1$ and 10 mm, respectively), while oxygen near 120 GHz ($\lambda \sim 2.5$ mm) and from 50 to 70 GHz ($\lambda \sim 5$ mm). Then, the atmosphere becomes nearly transparent for $\lambda > 15$ mm (20 GHz).

In the presence of particles (such as aerosols and/or hydrometeors forming clouds), their contribution to the extinction is a combination of both absorption and scattering which strongly depends on the size, composition, and chemical–physical properties of the particle.

Aerosols' optical depths are usually less than a tenth of unit and only reach comparatively large values (unity or greater) in case of smoke, dust storms, and severe pollution events. Conversely, clouds may easily achieve large optical depths. The contribution of clouds to extinction is almost purely scattering at shorter wavelengths, while it becomes strongly absorbing in the IR range. At longer wavelengths, the scattering contribution tends to become negligible, and also the absorption decreases substantially, so that clouds in the microwave region are rather, but not completely, transparent.

2.2.3 Atmospheric Emission

From the concept of an ideal black body and Kirchoff's law, it is known that the emission from a black body depends only on its temperature and that the higher the temperature of the body, the more is its emission. The spectral distribution of a blackbody emission is given by the Planck's law, which expresses the radiance $B_\lambda(T)$ emitted from a blackbody at temperature T and wavelength λ as

$$B_\lambda(T) = \frac{2hc^2}{\lambda^5}\frac{1}{(\exp(hc/\lambda kT) - 1)}, \tag{22}$$

where h and k are the Planck's and Boltzmann's constants, respectively. From simple consideration about Kirchoff's law, it is known that atmosphere both absorbs and emits radiation. Therefore, the same thin layer of ds thickness discussed above will emit radiation as

$$dI_{\text{emit}} = -dI_{\text{a}} = \beta_{\text{a}} B ds, \tag{23}$$

where we drop the wavelength λ index for convenience and thus B indicates the Planck function $B_\lambda(T)$. The net change in radiant intensity at the boundaries of the thin layer is given by the Schwartzschild's equation:

$$\frac{dI}{ds} = \beta_{\text{a}}(B - I). \tag{24}$$

This equation represents a fundamental description of radiative transfer equation (RTE) in a non-scattering medium, which is a reasonable approach for most of the problems involving IR and MW. This equation can be solved for the intensity reaching a sensor looking at a particular direction of propagation:

$$I(0) = I(\tau)e^{-\tau} + \int_{o}^{\tau} Be^{-\tau} d\tau. \tag{25}$$

Considering the case of a plane parallel non-scattering atmosphere and a sensor located at the surface, the RTE can be written as

$$I^{\downarrow}(0) = I^{\downarrow}(\infty)e^{-\tau(0,\infty)/\mu} + \int_{o}^{\infty} B(z)\frac{\beta_{\text{a}}(z)}{\mu}e^{-\tau(0,z)}dz, \tag{26}$$

where $z = \infty$ represents an arbitrary point beyond the top of the atmosphere. For sensors sensitive to flux rather than intensity, the flux at the surface is obtained simply by integrating the intensity over one hemisphere of solid angle:

$$F^{\downarrow}(0) = 2\pi \int_{0}^{1} I^{\downarrow}(0,\mu)\mu d\mu. \tag{27}$$

Finally, one may take this equation and simply integrate over wavelength to obtain broadband radiative flux at surface.

2.2.4 Radiative Transfer with Scattering

In the case where the atmosphere contains clouds and/or aerosols, the scattering source term in the radiative transfer equation becomes important; all of the above interactions, absorption, emission, scattering, and transmission will simultaneously take place, and their relative importance depends on wavelength, atmospheric composition, and the size, shape, and composition of the particles. In the situation considered here, namely upward-looking radiometers viewing an absorbing and scattering medium, the equation that relates the primary observable, radiance, to the atmospheric state becomes:

$$\mu \frac{dI(\mu,\phi)}{d\tau} = I(\mu,\phi) - J(\mu,\phi). \tag{28}$$

Here, the source function for both emission and scattering is a weighted sum of thermal emission and scattering from other directions, the single scattering albedo controlling the weight assigned to each term:

$$J(\mu,\phi) = (1-\omega)B + \frac{\omega}{4\pi} \int_{0}^{2\pi} \int_{-1}^{1} p(\mu,\phi;\mu',\phi') I(\mu',\phi') d\mu' d\phi', \tag{29}$$

where $\mu \equiv |\cos\vartheta|$, $\mu' \equiv |\cos\vartheta'|$, and $\vartheta, \phi, \vartheta', \phi'$ are the spherical angular coordinates of the incident and scattered radiation, respectively. Finally, the RTE in the presence of absorption, emission, and scattering for a plane parallel atmosphere is given by

$$\mu \frac{dI(\mu,\phi)}{d\tau} = I(\mu,\phi) - (1-\omega)B - \frac{\omega}{4\pi} \int_{0}^{2\pi} \int_{-1}^{1} p(\mu,\phi;\mu',\phi') I(\mu',\phi') d\mu' d\phi'. \tag{30}$$

3 Instrumentation

Radiometer is a generic term used to indicate all the passive instruments measuring radiation. There is a large variety of ground-based radiometric instruments that are used for atmospheric research and applications. Some instruments work in the shortwave range (UV to visible), other in the longwave range (IR to MW), some instruments observe radiation intensities, other fluxes of radiation, some in broad other in narrow to quasi-monochromatic bands. This section introduces just a few of these instruments, selecting those that are treated in the later chapters of this book. Since some of these are commercially available, we, of course, do not endorse any particular instrument.

3.1 Calibration

A key issue of radiometric instrument and observations is accurate calibration. In fact, the naturally emitted signal may be of the same order or even smaller than the noise emitted by the instrument itself. Thus, to derive quantitative information on the atmosphere from radiometric measurements, accurate calibration is required.

Some radiometric receivers have one or two internal noise sources that provide some measure of calibration. However, component losses, lack of complete knowledge of radiometric parameters, and a host of other causes usually dictate that some external calibration method also be employed. Assuming square law detectors, in which the output voltage is proportional to the input power, a seemingly straightforward calibration method is to view two external blackbody targets that are kept at two widely separated temperatures. Preferably, the target radiances bracket the range of radiances emitted from the scene. It is important to construct targets with high emissivity such that reflections from external sources are negligible and to have the targets sufficiently large to fill the instrument field of view. Targets are frequently constructed with a surface having high thermal conductivity covered with a thin layer of very absorbing material. The target is frequently embedded in a thermal insulator that is transparent to incoming radiation. Finally, when a target is placed in a thermal environment in which the environmental temperature differs greatly from desired target temperature, measurements of target temperatures at several locations within the target are essential.

The use of blackbody targets immersed in cryogenic fluids, such as liquid nitrogen (LN_2), is another commonly used method of establishing calibration (McGrath and Hewison, 2001; Cimini et al., 2003c). In this method, a blackbody target is immersed in the cryogen and the radiometer looks directly at the target. Allowance for the reflection of the ambient scene must be made, and the reflection coefficient of the cryogen must also be known.

For radiometers operating at transmission window wavelengths, the so-called tipping curve calibration method (or tipcal) can give a high degree of accuracy. In this method, brightness temperatures are measured as a function of elevation angle θ and are then converted to opacity $\tau(\theta)$ (Westwater, 1993). If the system is in calibration, then the linear fit of $\tau(\theta)$ as a function of optical air mass will pass through the origin; conversely, if the linear fit does not pass through the origin, then a single parameter in the radiometer equation is adjusted until it does. The most serious errors affecting this method are those caused by non-stratified atmospheric conditions and can occur due to clouds and horizontal variations in the water vapor field.

3.2 Pyrometers

The term pyrometer is generally used to indicate a remote sensing device that intercepts and measures broadband thermal radiation; the word pyrometer comes from the Greek words pyro (fire) and meter (to measure). A pyrometer consists of an optical system and a detector. The optical system focuses the thermal radiation onto the detector. The output signal of the detector is related to the irradiance [W/m^2] of the target through the Stefan–Boltzmann law. Depending on the range of wavelengths they are sensitive to, pyrometers may be used to measure direct and/or diffuse visible radiation, atmospheric, or ground IR radiation or to determine the temperature of an object's surface; in all these cases, the instruments acquire more specific names, as discussed below.

3.2.1 Pyrgeometer

A pyrgeometer is a device that measures the irradiance investing a plane surface detector and emitted by the Earth (geo in Greek) in a broad IR band that extends approximately from 4.5 to 100 μm. This is commonly used for measuring the incoming thermal radiation from the sky and clouds or the outgoing thermal radiation from the ground. The pyrgeometer thermopile detector measures the net radiation balance between the incoming and outgoing longwave radiation flux and converts it to a voltage according to $E_{\mathrm{net}} = U/S$ where E_{net} is the net radiation at sensor surface [W/m^2], U is the thermopile output voltage [V], and S is the sensitivity/calibration factor of instrument [V/W/m^2]. The value for S is determined during calibration of the instrument, which is performed at the production factory with a reference instrument traceable to a regional calibration center.

To derive the absolute downward longwave flux, the temperature of the pyrgeometer has to be taken into account. It is measured using a temperature sensor inside the instrument, near the cold junctions of the thermopile, and assuming the pyrgeometer to approximate a black body. Thus, it emits longwave radiation according to $E_{\mathrm{out}}=\sigma \cdot T^4$, where E_{out} is the longwave radiation emitted by the Earth's surface [W/m^2], σ is the Stefan–Boltzmann constant [W/(m^{2}K^4)], and T is the absolute temperature of pyrgeometer detector [K]. From the calculations above the incoming longwave radiation can be derived. This is usually done by rearranging the equations above to yield the so-called pyrgeometer equation:

$$E_{\mathrm{in}} = U/S + \sigma T^4. \tag{31}$$

As a result, the detected voltage and instrument temperature yield the total global longwave downward radiation.

Finally, the net longwave radiation can be calculated using two pyrgeometers, one looking up and one looking down, ideally mounted on the same plate such that the temperature of the pyrgeometers is the same and is irrelevant for the net radiation calculation.

3.2.2 Pyranometer

A pyranometer is a device used to measure broadband visible irradiance coming from the sky (*ano* in Greek) on a planar surface from a field of view of 180°. This irradiance contains of course both direct and diffuse solar radiation in a range extending approximately from 0.3 to 2.8 μm. Similarly to pyrgeometers, with two pyranometers, one pointing at zenith the other at nadir, it is possible to measure the net shortwave radiation: the upper sensor measures incoming global solar radiation and the lower sensor measures solar radiation reflected from the surface below.

Converting the two signal outputs to irradiance [W/m^2], the surface albedo (I_r/I_i) can be simply calculated; therefore such a system is also called albedometer.

3.2.3 Pyrheliometer

A pyrheliometer is an instrument designed specifically to measure the normal incidence direct beam solar irradiance. This is achieved by the shape of the collimation tube, always pointing orthogonally to the radiation beam the sun disk with a field of view limited to 5°, and by the quartz window acting as a filter that passes solar radiation only between 0.2 and 4 μm.

3.2.4 Infrared Thermometers

Instruments capable of measuring thermal radiation from an object and providing an output signal calibrated in temperature units are called radiation thermometers. In accordance with Planck's law, the radiances are clearly related to the temperatures, provided the relative spectral response is known. The output signal of a linear detector is proportional to the measured radiance, and thus it is possible to calibrate the output signal in temperature units (i.e., Kelvin).

A radiation thermometer measuring the radiance in an IR broad band is called IR thermometer (IRT). It provides measurements of the equivalent blackbody brightness temperature of the scene in its field of view. In this contest, IR thermometers are used to measure either the radiating temperature of the ground surface or the sky temperature in a given direction for detecting the presence of clouds. For calibration purposes, the IRT is placed in front of a blackbody calibration source (with known and high emissivity) whose temperature must be measured by means of a calibrated probe.

3.2.5 Examples

Kipp & Zonen CN1

Kipp & Zonen (http://www.kippzonen.com/) is marketing a range of net radiometers for the measurement of incoming and outgoing short- and longwave radiation. Moreover, Kipp & Zonen offers a variety of broadband radiometers measuring thermal radiation. All types are virtually maintenance-free and designed for continuous outdoor use. The main applications are in agrometeorology (evapo-transpiration and

Fig. I.1.3 Picture of the Kipp & Zonen CNR 1 net radiometer (*right*) and the MT5 microwave radiometer (*left*) during the outdoor deployment at ISSAOS 2007 in L'Aquila

crop damage prevention) and in climatology, meteorology, and hydrology for measurement of the radiation balance, and in renewable energy industry (heat exchange in thermal solar systems). The CNR 1 is a net radiometer combining two thermopile pyranometers for shortwave radiation measurements (including incoming solar radiation, reflected radiation, albedo, radiation balance) with two pyrgeometers for far infrared measurements (sky radiation, ground surface radiation, radiation balance) providing four separate signal outputs. The CNR 1 is very accurate and reliable and it is often used as the reference instrument for a network of lower performance net radiometers. A picture of the CNR 1 net radiometer deployed during the outdoor lectures at ISSAOS 2007 is shown in Fig. I.1.3.

3.3 Microwave Radiometers

A device measuring radiant intensity in discrete bands in the wavelength range from 10 cm to 0.5 mm is called a microwave radiometer (MWR). The MWRs commonly deployed for remote sensing of the troposphere use either single or multi-channel with frequency in the range between 10 and 400 GHz. The calibration of MWR relies on opportune combinations of internal noise sources, external targets, cryogenic loads, and tipping curve methods (Cimini et al., 2007a). The major advantage of microwave remote sensing is that even in the presence of thick clouds, fog, or drizzle, thermodynamical properties of the atmosphere can be determined with good accuracy. In the last decade, since it was recognized that the implementation of operational networks of microwave radiometers was hampered by the cost and complexity of the available instruments, a major objective has been to develop network-suitable low-cost and robust microwave radiometers. A short list of commercially available and commonly used MWR is given hereafter. More information on the hardware design, observations techniques, and applications of MWR is available in Janssen (1993) and Westwater et al. (2005).

3.3.1 Single-Channel Temperature Profiler

A single-channel MWR can be used for the retrieval of atmospheric temperature profiles in the atmospheric boundary layer (ABL) from 0 to 600 m above ground level. The technique consists of measuring atmospheric emission at different angles in a wavelength band that exhibits relatively high atmospheric attenuation. Usually this kind of MWRs operates near the peak of the strong oxygen band at 60 GHz (wavelength 5 mm). From the downwelling radiation at different elevation angles we can retrieve atmospheric air temperature gradients with respect to horizontal air temperature. In fact, the radiation in the horizontal direction can be used as a reference level since the brightness temperature (T_b) is essentially equal to the air temperature at the measurement height. Thus, an accurate air temperature measurement provides a calibration of the radiometer offset. The versatility and the robustness of the technique outline the potential of these instruments as a useful tool for integrated ground-based remote sensing systems.

3.3.2 Multi-Channel Temperature and Humidity Profilers

Atmospheric temperature and humidity profiles can be retrieved by multi-channel MWR observations. The set of channels is selected to observe atmospheric brightness temperatures in few frequency bands from 22 to 30 GHz, sensitive to water vapor and liquid water, and in few other bands from 51 to 59 GHz, sensitive to air temperature (Solheim et al., 1998; Ware et al., 2003; Rose et al., 2005).

MWR operating at higher frequencies (50–400 GHz) has been demonstrated to provide enhanced sensitivity and accuracy in the retrieval of humidity profiles in extremely dry environments (Cimini et al., 2007a). These instruments typically observe brightness temperatures in few channels from 51 to 59 GHz, sensitive to air temperature, few other channels around the 183.31 and/or 380.2 GHz water vapor absorption lines, plus few more channels in atmospheric windows, as at 90, 150, and 340 GHz.

3.3.3 Examples

Kipp & Zonen MTP5

Kipp & Zonen (http://www.kippandzonen.com) is marketing a radiometer that was originally designed and deployed by the Russian firm ATTEX (Kadygrov and Pick, 1998; Westwater et al., 1999). The radiometer is a single-channel (60 GHz) solid-state Dicke-type super-heterodyne receiver that is electronically chopped at 1 KHz between the sky and a reference noise source. The antenna is a scalar horn with a full-width-half-power (FWHP) beam width of 6º and scans by viewing a flat reflector at each of 11 scanning angles. Because of the 2 GHz bandwidth and a low receiver noise temperature of 600 K, a high sensitivity of 0.04 K is achieved. Calibration of the receiver is achieved by 0.1°C temperature control and a switched internal noise generator. A one-point absolute calibration is achieved either by viewing an external target or by knowing the emission temperature in the horizontal direction. A variation of this radiometer, developed at NOAA, scans continuously in a 360º vertical plane and, in addition to temperature profiles, can also be used to measure air–sea temperature difference (Trokhimovski et al., 1998; Cimini et al., 2003a–c). A picture of the MTP5 microwave radiometer deployed during the outdoor lectures at ISSAOS 2007 is shown in Fig. I.1.3.

Radiometrics MP-3000

Radiometrics Corporation (http://www.radiometrics.com) has developed a multi-frequency microwave radiometer that is based on a highly stable, tunable, and synthesized local oscillator in the receiver. This design overcomes errors caused by receiver frequency drift while allowing observation of a large number of frequencies across wide tuning ranges (currently 35). The total power receiver has a highly stable noise diode that is used as a gain reference. It also measures zenith infrared temperature, surface temperature, humidity, and pressure. The instrument is portable and has automated elevation- and azimuth-scanning capability, and the observation interval can be as short as several seconds (Fig. I.1.4).

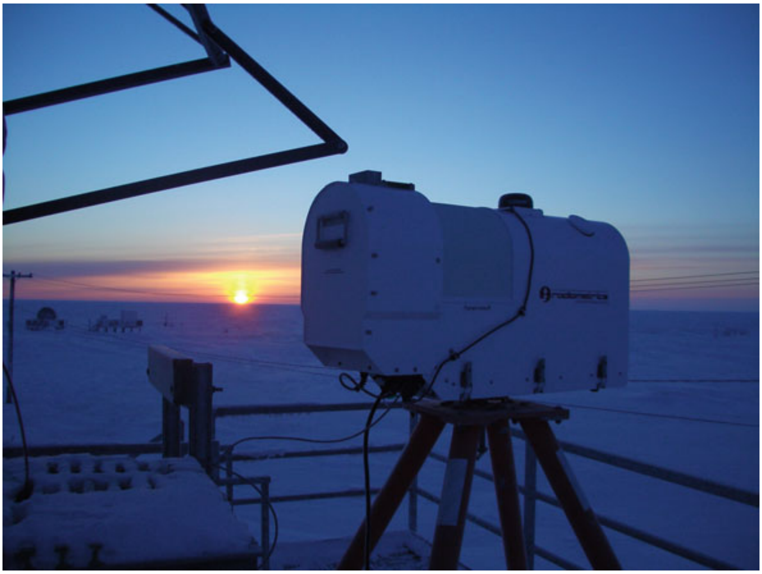

Fig. I.1.4 Picture of the Radiometrics MP-3000A, a multi-channel MWR for temperature and humidity profiling

RPG-HATPRO

The Radiometer Physics GmbH (http://www.radiometer-physics.de) is commercializing a 14-channel humidity and temperature profiler (RPG-HATPRO) from 22 to 60 GHz. The RPG-HATPRO comprises total-power radiometers utilizing direct detection receivers at all frequencies. The receivers of each frequency band are designed as filter banks in order to acquire each frequency channel in parallel. This approach avoids problems that might arise from mixers or local oscillators and possible interferences caused by communication systems that frequently operate near the IF frequencies. In addition, the flexibility to adjust each channel bandwidth individually allows for optimizing temperature profiling for both boundary layer and full troposphere.

3.4 Infrared Interferometers

A spectrometer in general is a device that measures radiant intensity as a function of wavelength. Fourier transform infrared (FTIR) spectroscopy is a passive technique for the observations of thermal radiation with high spectral resolution. FTIR radiometers measure the absolute infrared spectral radiance (W/m^2 st cm^{-1}) of the sky with a spectral range of typically 500–3,000 cm^{-1} (wavelength ~20–30 μm), a spectral resolution of the order of 1.0 cm^{-1}, and an instrument field of view of about 1°–2°. The instrument core is a Michelson interferometer, which allows the downwelling atmospheric emission in the entire bandwidth to be viewed simultaneously. Thus, FTIR spectrometers measure the interferogram of the EM spectrum of interest and a fast Fourier transform of the measured interferogram then yields the radiance spectrum. The advantages of the interferometric approach with respect to other spectral-resolving techniques (such as filters, grids) are multifold and can be summarized in the delivery of fast, simultaneous, fine, and accurately resolved radiance spectra.

Spectra observed from two blackbodies at known temperatures are used to calibrate the atmospheric spectrum (Revercomb et al., 2003). Two well-characterized blackbody targets are used, and a rotating gold-plated scene mirror is used to direct radiation from the target (either the sky or one of the blackbodies) into the interferometer. Collection of each spectrum takes few seconds, but averaging is performed to reduce random noise. Calibrated atmospheric spectra are typically available every few minutes (5 to 15), though rapid sampling mode is also available at 1 min temporal resolution (Demirgian and Dedecker, 2005). To estimate the uncertainty in the FTIR observation, uncertainties in the blackbody temperatures and emissivities must be propagated via the linear calibration equation to derive a root sum of square error in the observed spectrum (Knuteson et al., 2004b). The calibration procedure also accounts for detector nonlinearity, spectral calibration, including the removal of interferometer self-apodization effects and spectral scale normalization. Typical residuals of a side-by-side comparison of two instruments show radiance differences smaller than 0.5 mW/ m^2 st cm^{-1}.

In the last 2 decades, significant efforts have been spent for advancing FTIR interferometers toward an unattended instrument for 24/7 deployment. This requirement for 24/7 unattended operation leads to the implementation of hardware (e.g., mechanical coolers) and robust software. The state-of-the-art of operational FTIR has demonstrated radiometric accuracy of better than 1% of ambient radiance, with a reproducibility of better than 0.2%. The spectral calibration is known to be better than 1.5 ppm using known spectral positions of atmospheric lines.

The measured atmospheric IR spectra have a variety of applications, including the evaluation of line-by-line radiative transfer codes (Tobin et al., 1999), cloud and aerosol detection and quantification (Turner et al., 2003a), and the retrieval of vertical profiles of temperature and water vapor in the atmospheric boundary layer (Feltz et al., 2003).

3.4.1 Examples

AERI

The atmospheric emitted radiance interferometer (AERI) is a fully automated, ground-based, passive interferometer that measures high spectral resolution downwelling infrared radiance from 500 to 3,000 cm^{-1} (19–3.3 μm), developed by the University of Wisconsin—Madison (Revercomb et al., 2003). An extended range (ER) unit, reaching 25 μm (400 cm^{-1}), was developed for the study of the extremely dry atmosphere typical of the poles. The maximum optical path delay is approximately ±1 cm, resulting in a maximum unapodized spectral resolution of 0.5 cm^{-1}.

The calibration goal for the AERI is to observe downwelling atmospheric radiance with an accuracy of better than 1% of the ambient (near surface) radiance (Revercomb et al., 1993). The blackbodies are high-emissivity (greater than 0.995) targets that contain accurate National Institute of Standards and Technology (NIST) traceable temperature sensors. The temperature of one of the blackbodies is fixed at 60°C, while the other is allowed to float at the ambient temperature. One of the advantages to using an ambient calibration target is that much of the emission measured by the AERI is from the atmosphere very close to the instrument. Therefore, the calibration error is very small for temperatures very near the surface temperature.

More details on the AERI instrument, calibration, and the uncertainties in its observations are provided by Knuteson et al. (2004a, b). AERI observations are routinely acquired at ARM sites in tropical, mid-latitude, and Arctic environments.

EISAR

The emission infrared spectrometer for atmospheric research (EISAR) belongs to the German Meteorological Service (DWD) and it is used for routine observations at the Lindenberg Meteorological Observatory as part of their atmospheric long-term monitoring commitment (Reichardt and Güldner, 2009). Its detector offers an effective spectral range from 600 to 3,000 cm^{-1} with a maximum spectral resolution of 0.3 cm^{-1}. A typical EISAR observation starts with a view to a calibration wide-aperture blackbody set to a temperature 5°C above the dew point, then it performs a series of sky measurements, and finally it concludes with a view to the blackbody set to a temperature of about 50°C. The two blackbody reference spectra are used to correct the detector nonlinearities and thus to achieve the radiometric precision of 0.1 K and accuracy of 1.0 K. Calibrated atmospheric spectra are collected once every 15 min, though a rapid sampling mode is also possible at 1-min resolution.

4 Retrieval Techniques

Techniques to derive meteorological information from radiation measurements are generally based on the radiative transfer equation (RTE) in Eq. (30) or its linearized perturbation form. Because only a finite number of imperfect radiation measurements are available, and a continuum of parameters is needed to describe atmospheric profiles, a rigorous mathematical solution does not exist and the inverse problem is said to be ill-posed (Twomey, 1977). Therefore, it is better to regard the measurements as constraints and to blend them with supplementary sources of information or to drastically reduce the dimensionality of the inverse problem by projecting the profiles onto their linear functionals. Useful supplementary information can be provided by a priori information obtained from past data or by model simulations.

The RTE can be approximated by a Fredholm integral equation of the first kind (Rodgers, 2000) and in its discrete form is written as

$$g_{\mathrm{e}} = Kf + \varepsilon, \tag{32}$$

where g_{e} is a vector composed of n measurements, f is an m-vector whose components represent the atmospheric parameters that we want to determine, K is an $n \times m$ matrix relating the measurements to the unknowns, and the n-vector ε explicitly denotes that the measurements have an unknown error component that will affect the solution to some degree. For mildly nonlinear problems, the perturbation form expressed is frequently used as the basis of subsequent iterations.

An excellent review article discussing techniques for solving the above Eq. (32) was written by Rodgers (1976) and further insights are given in Rodgers (2000). Many retrieval methods are used to solve Eq. (32), and we mention just a few frequently used in ground-based applications: statistical regression (Westwater, 1993), neural network inversion (Solheim et al., 1998), and Kalman filtering (Han et al., 1997). Finally, another technique developed in the last decade and of great promise is to combine radiometer data with a numerical forecast model (Löhnert et al., 2004; Hewison, 2007; Cimini et al., 2009).

5 Radiometric Sensing of Atmospheric Variables

This section provides a list of some selected applications of radiometric remote sensing to the monitoring of atmospheric variables that are important for meteorology, climatology, and weather hazards.

5.1 Energy Balance

The radiative equilibrium temperature of the Earth is determined by the balance between the energy absorbed from the sun and that emitted by the planet in the infrared. Climate studies and cloud/radiation interaction require breaking the Earth's energy budget down into its components. The radiative balance at the Earth surface is played by broadband shortwave (solar) and longwave (atmospheric/ground) irradiances with both their downwelling and upwelling components. Therefore, an integrated station for monitoring the total radiative flux exchange may be assembled

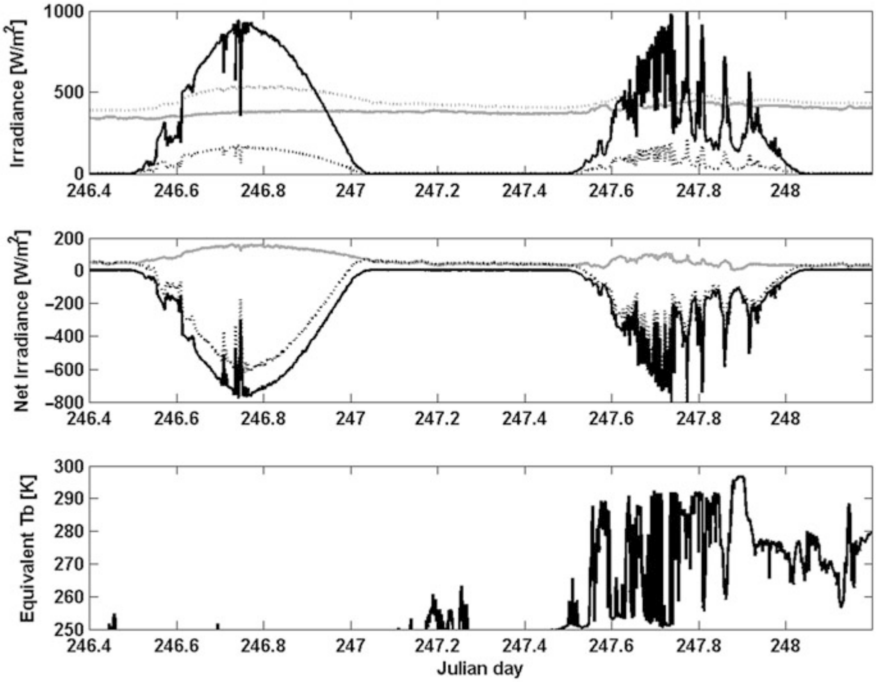

Fig. I.1.5 *Top*: Observations of shortwave (*black*) and longwave (*grey*) downwelling (*solid*) and upwelling (*dotted*) irradiances. *Center*: Total net irradiance (*dotted*) and net shortwave (*black*) and longwave (*grey*) irradiances. *Bottom*: Observations of sky temperature by an IRT indicate that day 246 was mainly cloud-free, while day 247 was prevalently cloudy (data courtesy of the ARM program) using pyranometers, pyrgeometers, and pyrheliometers, providing continuous measurements of as many components as possible:

- Pyrheliometer: direct normal shortwave (solar beam)
- Pyranometers: global horizontal shortwave (total hemispheric), diffuse horizontal shortwave (no direct component), and upwelling shortwave (reflected)
- Pyrgeometers: downwelling longwave (atmospheric emission) and upwelling longwave (ground emission)

A time series of observed shortwave and longwave downwelling and upwelling irradiances at mid-latitude in fall is shown in Fig. I.1.5. The time series is extending for almost two complete days and thus it shows the diurnal cycle of solar insulation. Note that the first day was mainly cloud-free while the second day was prevalently cloudy as confirmed by the corresponding IRT sky temperature. The net shortwave and longwave irradiances are shown, which contribute to the total net radiation received by the Earth's surface; shortwave energy accumulated throughout the day is released by outgoing longwave radiation during the night. Considering the two pyranometers, one pointing at zenith the other at nadir, measuring the global shortwave irradiance it is possible to measure the net shortwave radiation and the surface albedo (I_r/I_i): the upper sensor measures incoming global solar radiation and the lower sensor measures solar radiation reflected from the surface below.

5.2 Integrated Contents of Water Vapor and Cloud Liquid Water

Both water vapor and cloud liquid are important variables in meteorology and climate. Due to thermodynamic processes of evaporation and condensation, as well as transport by winds, these quantities vary greatly in space and time. Water vapor is characterized by density as a function of spatial coordinates and time. Water vapor density is limited, depending on temperature, such that the relative humidity is in the range of 0–100%.

Dual-frequency measurements of brightness temperature at an optimum frequency near the 22.235 GHz water vapor line and in a transmission window have been used to measure the integrated water vapor (IWV) and liquid water path (LWP) for about 25 years (Hogg et al., 1983). This technique relies on the fact that the two channels respond in substantially different ways to IWV and LWP, so that the opacity contribution of these constituents can be separated with as little ambiguity as possible. Indeed, although both channels are sensitive to both IWV and LWP, the channel near 22.2 GHz has a proportionally larger response to IWV, while the reverse is true for the window channel. In particular, the water vapor channel is usually selected at one of the two so-called hinge points (Cimini et al., 2003a–c), where the pressure (i.e., height) dependence is minimized and thus the radiance is sensitive entirely to the integrated amount. For the retrieval of IWV, the window channel corrects for the changing LWP in the atmosphere. Similarly, the liquid water path can be estimated from atmospheric emission measurements in the microwave region because in this spectral region, the cloud contribution strongly increases with frequency. For the retrieval of LWP, the channel close to the water vapor absorption line corrects for the changing water vapor concentration of the atmosphere.

The general accuracy of dual-frequency radiometric measurement of IWV has been shown to be better than 1 mm rms (Revercomb, 2003). Because of the lack of in situ measurements of cloud liquid, an adequate experimental evaluation of LWP over a range of cloud conditions is not available. The estimated accuracy for LWP retrievals is of the order of 25 g/m^2, of which about 10 g/m^2 is attributed to the measurement error while the rest can be attributed to the underdetermined retrieval problem. An example of IWV and LWP retrievals taken during the 2004 Arctic Winter Radiometric Experiment (Westwater et al., 2004) at the atmospheric radiation measurement (ARM) site in Alaska is shown in Fig. I.1.6.

The accuracy of IWV and LWP retrievals can be enhanced by using higher frequency channels, typically 90 and 183 GHz, as demonstrated for dry environments in the Arctic (Cimini et al., 2007b).

Improvements on the dual-channel method can be made with multi-frequency observations. For example, the additional use of the 90 GHz channel further constrains the LWP retrieval problem and improves its accuracy to less than 15 g/m^2

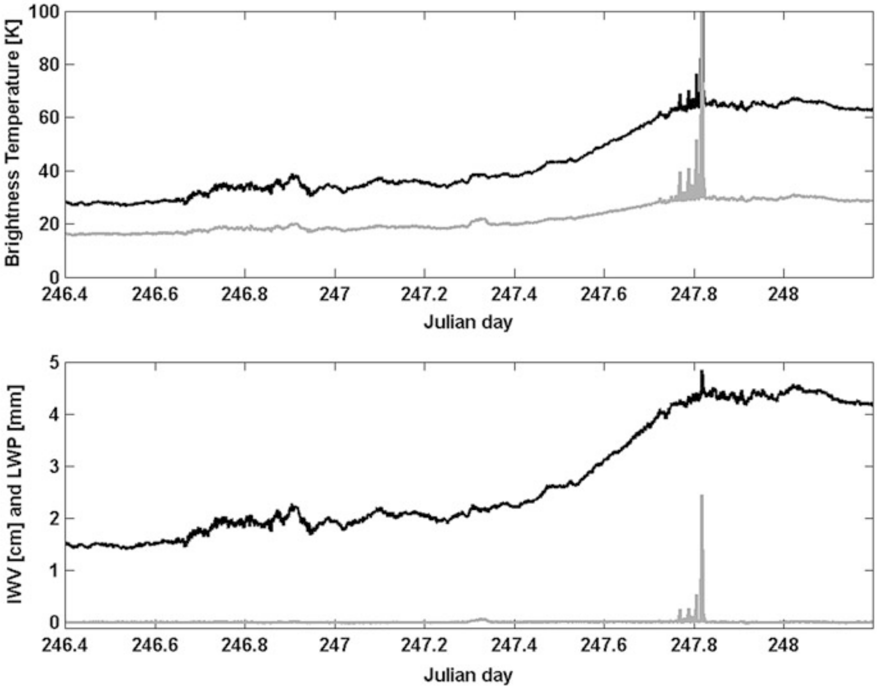

Fig. I.1.6 *Top*: Time series of brightness temperatures from a dual-channel MWR at 23.8 GHz (*black*) and 31.4 GHz (*grey*). *Bottom*: Corresponding IWV (*black*) and LWP (*grey*) (data courtesy of the ARM program)

(Crewell and Löhnert, 2003). Another recently developed method relies on the synergy of MWR and FTIR observations (Turner, 2007).

5.3 Boundary Layer Temperature Profiling from Scanning Observations

Angular techniques for measuring emission were developed by NOAA in the early 1970s (Westwater et al., 1975), but due to mechanical simplicity, the zenith-viewing multi-spectral radiometers were commonly deployed. However, in 1992, Russian scientists developed a scanning single-channel radiometer for routine monitoring of the boundary layer (Kadygrov and Pick, 1998). From the downwelling radiation at different elevation angles, atmospheric air temperature profiles can be obtained. As a simple way of explaining the technique, we know that for a constant absorption coefficient, for horizontally stratified atmosphere, and for temperature profile that changes linearly with height, the brightness temperature is equal to the air temperature at the position where the opacity is equal to 1. For more complex profiles, an inversion method must be used. The vertical resolution of the retrieved profiles is a function of altitude and ranges from about 10 m near the surface to about 300 m at the 500 m altitude. The retrieval accuracy (rms error) was shown to be better than 0.5 K below 500 m. Because of the simplicity and portability of the instrument and its extremely flexible characteristics, it has been used from airborne, ship-, and ground-based platforms (Westwater et al., 1999; Cimini et al., 2003a–c; Leuskii et al., 2000). An example of temperature profiles retrieved by such a single-channel radiometer during the NAURU99 field campaign (Cimini et al., 2003a–c) is shown in Fig. I.1.7.

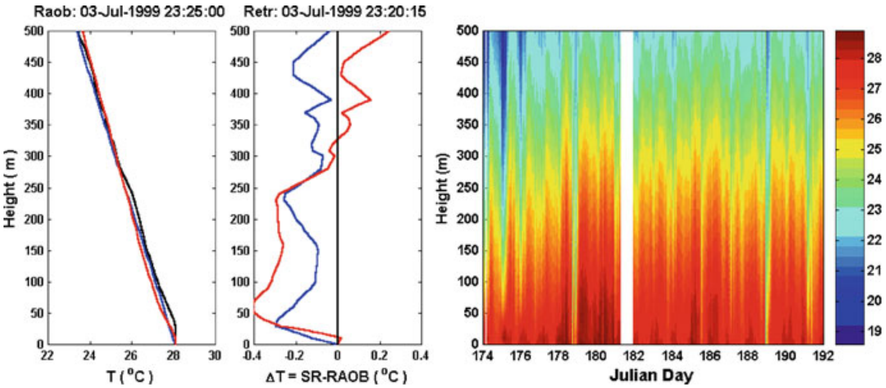

Fig. I.1.7 Boundary layer temperature profiles as measured by a radiosonde and retrieved by two independent single-channel scanning radiometers (*left*). Temperature residual between retrievals and radiosonde (*center*). Two-week time–height time series of temperature profiles (°C) retrieved by a single-channel scanning MWR (*right*) in the tropics

5.4 Temperature and Humidity Profiling by Multi-Frequency Observations

Radiometric temperature and humidity profiling can be accomplished by measuring the spectrum of radiation intensity at points along the side of an absorption line (Westwater et al., 1993). By scanning outward from the band center, where the opacity is larger, onto the wings of the band, where the radiometer “sees” deeper (higher) into the atmosphere, altitude information is obtained. Either shoulder of the band center is suitable for retrieval of temperature and humidity profiles information. Emission at any altitude is proportional to local temperature and abundance of the absorbing gas; channels close to water vapor lines (22.2 GHz, 183.2 GHz) are then used for humidity profile retrievals, while in case the absorbing gas has constant concentration, as for example for oxygen, the temperature profile can be retrieved.

Temperature and humidity profiles are estimated from radiometric observations by means of inversion methods, relying on a priori information on the statistics of

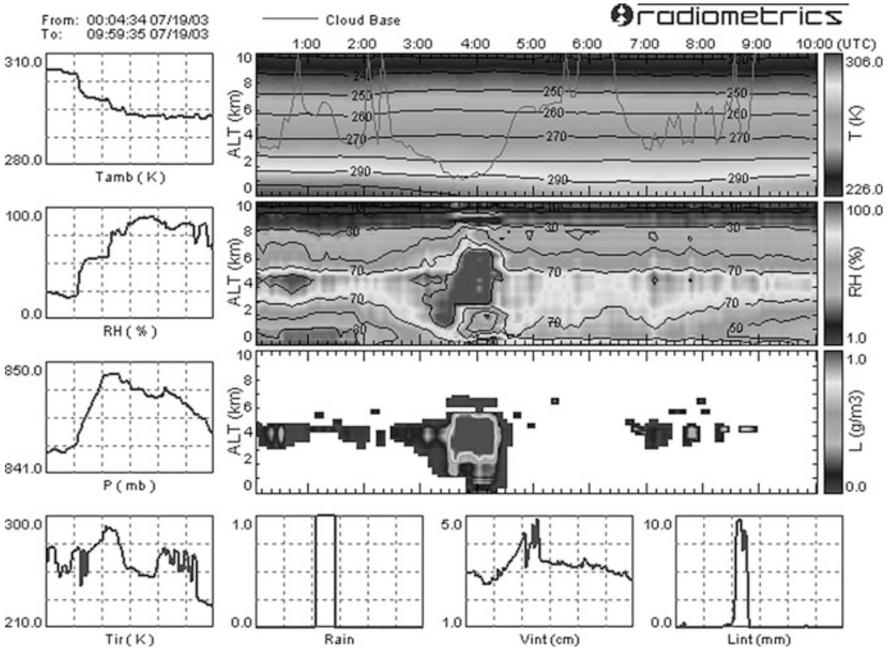

Fig. I.1.8 Screenshot of the real-time output from the Radiometrics MP-3000. Plots refer to data collected during July 19, 2003, in Boulder, CO, USA. A rain shower happened roughly at 0400 UTC. Contour plots show time–height cross sections of atmospheric temperature (*top*), relative humidity (*middle*), and liquid water (*bottom*). Surface temperature, relative humidity, and pressure are shown on the *left*. Infrared cloud temperature, rain detection, integrated content of vapor and liquid are shown on the *bottom* the field to be retrieved. Historical radiosonde and neural network or regression are usually used for profile retrieval (Ware et al., 2003); more recently, variational methods have been developed to combine radiometer data with numerical forecast model output (Löhnert et al., 2004; Hewison, 2007; Cimini et al., 2009). Comparisons between radiosondes and retrieved profiles in the lower troposphere are shown in Güldner and Spänkuch (2001) and Cimini et al. (2006) and demonstrate that temperature and humidity retrieval accuracy is best near the surface and degrades with height to <1.5 K, < 0.7 g/m3, respectively. A screenshot of the real-time output of a commercial MWR profiler is shown in Fig. I.1.8.

Profile retrievals from MWR have much coarser vertical resolution than radiosonde soundings, especially above the boundary layer, but have temporal resolutions of minutes. Retrieval error is smaller than radiosonde sounding error for boundary layer temperatures and higher above the boundary layer. The dominant radiosonde error is the representativeness error that results from the characterization of a model cell volume by a point measurement. This type of error is especially important when there are strong temporal or horizontal spatial gradients in the meteorological profiles. Radiometric retrievals can be temporally averaged and in these strong gradient (temporal or horizontal) conditions may be less susceptible to representativeness error than radiosonde soundings.

Note that in clear-sky conditions, vertical profiles of temperature and water vapor in the atmospheric boundary layer can be retrieved by FTIR spectral observations. Due to the high spectral resolution of FTIR observed spectra, the optimal vertical resolution is of the order of 100 m in the atmospheric boundary layer (up to ~3 km) (Feltz et al., 2003).

6 Conclusions

Surface-based radiometry has provided useful data on energy budget, temperature, water vapor, clouds, and other atmospheric constituents. Steady progress has been made in the development of robust, sensitive, and accurate instrumentation. This has been accompanied by continued development of suitable forward and inverse models for the accurate calculation of radiation intensity and the retrieval of atmospheric parameters. The advances in forward modeling positively affect surface-, airborne-, and satellite-based remote sensing, as well as telecommunication.

It now seems likely that assimilation of data with forecast models is a very promising technique for exploiting radiometer data (Nehrkorn and Grassotti, 2004). Of equal promise is the synergism of active and passive sensors as has been achieved in cloud sensing (Löhnert et al., 2001), in moisture profiling (Stankov et al., 1996; Han and Westwater, 1995), and in the use of wind profiler estimates of significant moisture gradients to improve humidity profile retrieval (Bianco et al., 2005). All the above topics will be discussed in the second part of this volume.

References

Battaglia A, Saavedra P, Rose T, Simmer, C (2009) Rain observations by a multifrequency dual polarized radiometer. IEEE Geosci Remote Sens Lett 6(2):354–358

Bianco LD, Cimini FS, Marzano, Ware R (2005) Combining microwave radiometer and wind profiler radar measurements for high-resolution atmospheric humidity profiling. J Atmos Oceanic Tech 22:949–965, July 2005

Cimini D, Hewison TJ, Martin L, Güldner J, Gaffard C, Marzano FS (2006) Temperature and humidity profile retrievals from ground-based microwave radiometers during TUC. Meteorol Zeitschrift 15(1):45–56

Cimini D, Shaw JA, Han Y, Westwater ER, Irisov V, Leuski V, Churnside JH (2003a), Air temperature profile and air-sea temperature difference measurements by infrared and microwave scanning radiometers. Radio Sci 38(3):8045. doi:10.1029/2002RS002632

Cimini D, Westwater ER, Han Y (2003b) Theoretical analysis of the frequency allocation of the hinge points around 22.235 GHz. In: Proceedings of the 13th ARM Science Team Meeting, Broomfield, Colorado, 31 March–4 April 2003

Cimini D, Westwater ER, Han Y, Keihm SJ (2003c) Accuracy of ground-based microwave radiometer and balloon-borne measurements during the WVIOP2000 field experiment. IEEE Trans Geosci Remote Sens 41(11):2605–2615

Cimini D, Westwater ER, Gasiewski AJ, Klein M, Leusky V, Dowlatshahi S (2007a) The ground-based scanning radiometer: a powerful tool for study of the arctic atmosphere. IEEE Trans Geosci Remote Sens 45(9):2759–2777

Cimini D, Westwater ER, Gasiewski AJ, Klein M, Leusky V, Liljegren J (2007b) Ground-based millimeter- and submillimeter-wave observations of low vapor and liquid water contents. IEEE Trans Geosci Remote Sens 45(7):2169–2180

Cimini D, Westwater ER, Gasiewski AJ (2009) Temperature and humidity profiling in the Arctic using millimeter-wave radiometry and 1DVAR. IEEE Trans Geosci Remote Sens. doi:10.1109/TGRS.2009.2030500

Clothiaux EE, Ackerman TP, Mace GG, Moran KP, Marchand RT, Miller MA, Martner BE (2000) Objective determination of cloud heights and radar reflectivities using a combination of active remote sensors at the ARM CART sites. J Appl Meteorol 39(5):645–665

Clough SA, Shephard MW, Mlawer EJ, Delamere JS, Iacono MJ, Cady-Pereira K, Boukabara S, Brown PD (2005) Atmospheric radiative transfer modeling: a summary of the AER codes. J Quant Spectros Radiative Transfer 91:233–244

Crewell S, Löhnert U (2003) Accuracy of cloud liquid water path from ground-based microwave radiometry. Part II. Sensor accuracy and synergy. Radio Sci 38(3):8042. doi:10.1029/2002RS002634

Elachi C (1987) Introduction to the physics and techniques of remote sensing, Wiley, New York, NY, p 444

Demirgian J, Dedecker R (2005) Atmospheric emitted radiance interferometer handbook, ARM TR-054. http://www.arm.gov/publications/tech_reports/handbooks/aeri_handbook.pdf. Accessed on Jan 2005

Feltz WF, Howell HB, Knuteson RO, Woolf HM, Revercomb HE (2003) Near continuous profiling of temperature, moisture, and atmospheric stability using the atmospheric emitted radiance interferometer (AERI). J Appl Meteorol 42:584–597

Goody RM, Yung YL (1995) Atmospheric radiation: theoretical basis, 2nd edn. Oxford University Press, New York, NY, pp 519

Güldner J, Spänkuch D (2001) Remote sensing of the thermodynamic state of the atmospheric boundary layer by ground-based microwave radiometry. J Atmos Ocean Technol 18:925–933

Han Y, Westwater ER (1995) Remote sensing of tropospheric water vapor and cloud liquid water by integrated ground-based sensors. J Atmos Ocean Technol 12(5):1050–1059

Han Y, Westwater ER, Ferrare RA (1997), Applications of Kalman filtering to derive water vapor from raman lidar and microwave radiometers. J Atmos Ocean Technol 14(3):480–487

Hewison T (2007) 1D-VAR retrievals of temperature and humidity profiles from a ground-based microwave radiometer, IEEE TGRS 45(7):2163–2168

Hogg DC, Decker MT, Guiraud FO, Earnshaw KB, Merritt DA, Moran KP, Sweezy WB, Strauch RG, Westwater ER, Little CG (1983) An automatic profiler of the temperature, wind and humidity in the troposphere. J Appl Meteorol 22(5):807–831

Janssen MA (1993) An introduction to the passive remote sensing of atmospheres. In: Michael A. Janssen (ed), Atmospheric remote sensing by microwave radiometry. Wiley, New York, NY, pp 1–36

Kadygrov EN, Pick DR (1998) The potential performance of an angular scanning single channel microwave radiometer and some comparisons with in situ observations. Meteorol Appl 5: 393–404

Knuteson RO et al (2004a) Atmospheric emitted radiance interferometer (AERI). Part I: Instrument design. J Atmos Ocean Technol 21(December):1763–1776

Knuteson RO et al (2004b) Atmospheric emitted radiance interferometer (AERI). Part II: Instrument performance. J Atmos Ocean Technol 21(December):1777–1789

Leuskii V, Irisov V, Westwater E, Fedor L, Patten B (2000) Airborne measurements of the sea-air temperature difference by a scanning 5-mm wavelength radiometer. In: Proceedings of IGARSS2000, Honolulu, 24–28 July 2000, pp 260–262

Liebe HJ (1989) MPM, an atmospheric millimeter wave propagation model. Int J Infrared Millimeter Waves 10(6):631–650

Liebe HJ, Hufford GA, Manabe T (1991) A model for the complex permittivity of water at frequencies below 1 THz. Int J Infrared Millimeter Waves 12(7):659–675

Liou K-N (1980) An introduction to atmospheric radiation. Academic Press, New York, NY, pp 392

Löhnert U, Crewell S, Simmer C (2004) An integrated approach toward retrieving physically consistent profiles of temperature, humidity, and cloud liquid water. J Appl Meteorol 43:1295–1307

Löhnert U, Crewell S, Macke A, Simmer C (2001) Profiling cloud liquid water by combining active and passive microwave measurements with cloud model statistics. J Atmos Ocean Technol 18:1354–1366

Marzano F, Cimini D, Ciotti P, Ware R (2005) Modeling and measurements of rainfall by ground-based multispectral microwave radiometry. IEEE Trans Geosci Remote Sens, 43:1000–1011

McGrath A., Hewison T (2001) Measuring the accuracy of MARSS – an airborne microwave radiometer. J Atmos Ocean Technol, 18:2003–2012

Nehrkorn T, Grassotti C (2004) Mesoscale variational assimilation of profiling radiometer data. In: 16th conference on numerical weather prediction. American Meteorological Society, Seattle, WA

Petty GW (2006) A first course in atmospheric radiation, 2nd edn. Sundog Publishing, Madison. pp 460. ISBN-10: 0-9729033-1-3

Philipona, R, Frohlich C, Betz Ch (1995) Characterisation of pyrgeometers and the accuracy of atmospheric long-wave radiation measurements. Appl Opt 34:1598–1605

Reichardt J, Güldner J (2009) Fourier transform infrared radiometer. In: Engelbart D, Monna W, Nash J, Matzler C (eds) EUR 24172 – COST Action 720 final report. Cost office, Brussels, pp 95–103

Revercomb HE, Turner DD, Tobin DC, Knuteson RO, Feltz WF, Bannard J, Bosenberg J, Clough S, Cook D, Ferrare R, Goldsmith J, Gutman S, Halthorne R, Lesht B, Liljegren J, Linne H, Michalsky J, Morris V, Porch W, Richardson S, Schmid B, Splitt M, Van Hove T, Westwater E, Whiteman D (2003) The ARM programs's water vapor intensive observation periods: overview, initial accomplishments, and future challenges. Bull Am Meteorol Soc 84(1):217–236

Rodgers CD (1976) Retrieval of atmospheric temperature and composition from remote measurements of thermal radiation. Rev Geophys Space Phys 14:609–624

Rodgers CD (2000) Inverse methods for atmospheric sounding: theory and practice. World Scientific, Singapore

Rose T, Crewell S, Löhnert U, Simmer C (2005) A network suitable microwave radiometer for operational monitoring of the cloudy atmosphere. Atmos Res 75(3):183–200, May

Rosenkranz PW (1998) Water vapor microwave continuum absorption: a comparison of measurements and models. Radio Sci 33(4):919–928

Solheim F, Godwin J, Westwater E, Han Y, Keihm S, Marsh K, Ware R (1998) Radiometric profiling of temperature, water vapor, and liquid water using various inversion methods. Radio Sci 33:393–404

Stankov BB, Westwater ER, Gossard EE (1996) Use of wind profiler estimates of significant moisture gradients to improve humidity profile retrieval. J Atmos Ocean Technol 13(6):1285–1290

Stephens GL (1994) Remote sensing of the lower atmosphere – an introduction. Oxford University Press, New York, NY, p 523

Tobin DC et al (1999) Downwelling spectral radiance observations at the SHEBA ice station: water vapor continuum measurements from 17 to 26 microns. J Geophys Res 104(D2):2081–2092

Trokhimovski YG, Westwater ER, Han Y, Leuskiy VY (1998) The results of air and sea surface temperature measurements using a 60 Ghz microwave rotating radiometer. IEEE Trans Geosci Remote Sens 36(1):3–15

Turner DD (2007) Improved ground-based liquid water path retrievals using a combined infrared and microwave approach. J Geophys Res 112 (D15204):15. doi: 10.1029/2007JD008530

Turner DD, Ackerman SA, Baum BA, Revercomb HE, Yang P (2003a) Cloud phase determination using ground-based AERI observations at SHEBA. J Appl Meteorol 42:701–715

Turner D, Lesht B, Clough A, Liljegren J, Revercomb H, Tobin D (2003b) Dry bias and variability in Väisälä RS80-H radiosondes: the ARM experience. J Atmos Ocean Technol 20(1):117–132

Twomey S (1977) Introduction to the mathematics of inversion in remote sensing and indirect measurements. Elsevier, New York, NY

Ware R, Carpenter R, Güldner J, Liljegren J, Nehrkorn T, Solheim F, Vandenberghe F (2003) A multi-channel radiometric profiler of temperature, humidity and cloud liquid. Radio Sci 38(4):8079–8032

Westwater ER (1993) Ground-based microwave remote sensing of meteorological variables. In: Michael A. Janssen (ed) Atmospheric remote sensing by microwave radiometry. Wiley, New York, NY, pp 145–213

Westwater ER, Crewell S, Matzler C (2005) Surface-based microwave and millimeter wave radiometric remote sensing of the troposphere: a tutorial. IEEE Geosci Remote Sens Newslett 16–33(March). ISSN 0161-7869

Westwater ER, Snider JB, Carlson AC (1975) Experimental determination of temperature profiles by ground-based microwave radiometry. J Appl Meteorol 14(4):524–539

Westwater ER, Han Y, Irisov VG, Leuskiy V, Kadygrov EN, Viazankin SA (1999) Remote sensing of boundary-layer temperature profiles by a scanning 5-mm microwave radiometer and RASS: comparison experiment. J Atmos Ocean Technol 16(7):805–818

Westwater ER, Klein M, Leuski V, Gasiewski AJ, Uttal T, Hazen DA, Cimini D, Mattioli V, Weber BL, Dowlatshahi S, Shaw JA, Liljegren JS, Lesht BM, Zak BD (2004) The 2004 north slope of Alaska arctic winter radiometric experiment. In: Proceedings of 14th Atmospheric Radiation Measurement (ARM) Science Team Meeting, April, 2004